ERDC/ITL TR-24-7

Information Technology Laboratory

US Army Corps of Engineers®
Engineer Research and Development Center

ERDC
ENGINEER RESEARCH & DEVELOPMENT CENTER

Mesoscale Multiphysics Simulations of the Fused Deposition Additive Manufacturing Process

Jeff Allen and Guillermo Riveros

May 2024

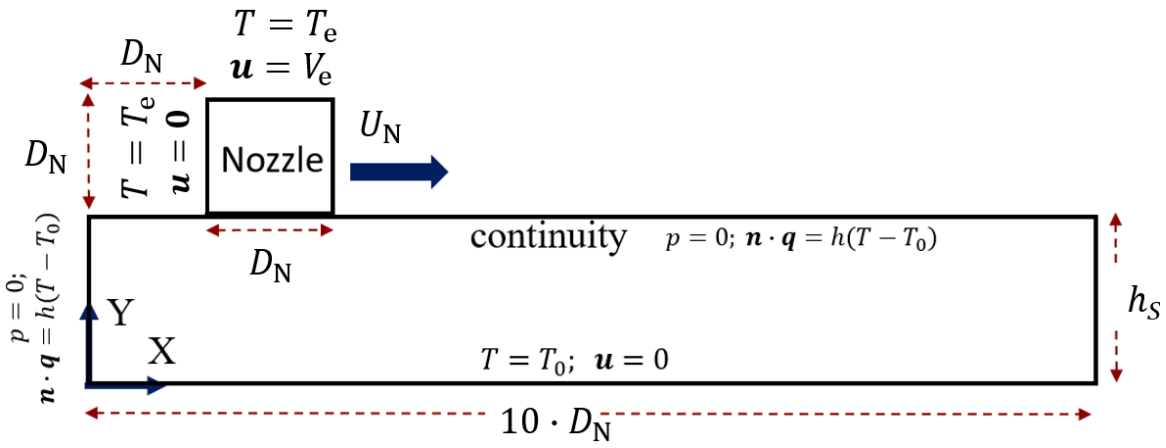

The U.S. Army Engineer Research and Development Center (ERDC) solves the nation's toughest engineering and environmental challenges. ERDC develops innovative solutions in civil and military engineering, geospatial sciences, water resources, and environmental sciences for the Army, the Department of Defense, civilian agencies, and our nation's public good. Find out more at www.erdc.usace.army.mil.

To search for other technical reports published by ERDC, visit the ERDC online library at https://erdclibrary.on.worldcat.org/discovery.

ERDC/ITL TR-24-7
May 2024

Mesoscale Multiphysics Simulations of the Fused Deposition Additive Manufacturing Process

Jeff Allen and Guillermo Riveros

US Army Engineer Research and Development Center (ERDC)
Information Technology Laboratory (ITL)
3909 Halls Ferry Road
Vicksburg, MS 39180-6199

Final Technical Report (TR)

Prepared for US Army Engineer Research and Development Center
Information Technology Laboratory
3909 Halls Ferry Rd
Vicksburg, MS 39180-6199

Under Funding Account Code U4393864, AMSCO Code 633043DC300

Abstract

As part of an ongoing effort to better understand the multiscale effects of fused deposition additive manufacturing, this work centers on a multiphysics, mesoscale approach for the simulation of the extrusion and solidification processes associated with fused deposition modeling. Restricting the work to a single line scan, we focus on the application of polylactic acid. In addition to heat, momentum, and mass transfer, the solid–liquid–vapor interface is simulated using a front-tracking, level-set method. The results focus on the evolving temperature, viscosity, and volume fraction and are cast within a set of parametric studies to include the nozzle and extrusion velocities as well as the extrusion temperature. Among other findings, it was observed that fused deposition modeling can be effectively modeled using a front-tracking method (i.e., the level-set method) in concert with a moving mesh and temperature-dependent porosity function.

Contents

Figures and Tables

Figures

Tables

Preface

This study was conducted for the Mantech to Manufacturing Science and Technology Program under High Performance Computing for Large Scale Additive Manufacturing, for which Dr. James Stinson was the program manager. The investigation was conducted under work unit "Innovative Hybrid Simulation and Design-by-Analysis Methods for Large Scale Additive Manufacture (AM) Structural Systems for Military and Civil Work Infrastructures," Funding Account Code U4393864, AMSCO Code 633043DC300.

This work was performed by the Computational Analysis Branch of the Computational Science and Engineering Division, US Army Engineer Research and Development Center, Information Technology Laboratory (ERDC-ITL). At the time of publication, Mr. David Stuart was branch chief; Dr. Jeffrey L. Hensley was division chief; and Dr. Robert M. Wallace was the technical director for Engineered Resilient Systems. The deputy director of ERDC-ITL was Dr. Jackie S. Pettway, and the director was Dr. David A. Horner.

COL Christian Patterson was commander of ERDC, and Dr. David W. Pittman was director.

This page intentionally left blank.

1 Introduction

Of the various forms of additive manufacturing, extrusion-based approaches such as fused deposition modeling (FDM) and fused filament fabrication have become very popular (Turner et al. 2014). The attraction to FDM is primarily due to its high reliability, low maintenance, large variety of applicable filament materials, and low initial investment cost (Turner et al. 2014). FDM is known to work with a variety of different polymers, such as acrylonitrile butadiene styrene and polylactic acid (PLA), as well as polymer matrix composites, polymer ceramic composites, nanocomposites, and fiber-reinforced composites (Mohan et al. 2017).

The primary liabilities associated with the FDM process typically relate to poor product quality and inconsistent reproduction efforts, which arise from various defects, including void formations, surface roughness, and inadequate bonding between layers. To some degree, these defects can be managed by proper control of the processing parameters (e.g., scan speed, feed velocity, injection temperature, etc.), but in many instances an additional pre- or post-treatment is required (i.e., chemical, heat, laser, or ultrasound) (Wickramasinghe et al. 2020).

1.1 Background

While there have been a large number of experimental studies related to various aspects of FDM, including the potential for defect mitigation (Sun et al. 2003; Ziemian et al. 2012; Nikzad et al. 2011), complementary theoretical/numerical studies are comparatively few in number and offer considerable avenues for advancement in the field. Typically, the numerical studies incorporate a thermodynamic or thermomechanical analysis and are developed for the meso- and macroscales using the finite element method (FEM). Some studies, for example, have focused on the inner flow dynamics of the nozzle (Ramanath et al. 2007; Mostafa et al. 2009), while other, more complicated models have attempted simulations of the extrusion and deposition process (Heller et al. 2016; Comminal et al. 2018; Serdeczny et al. 2018; Xia et al. 2017). These latter simulations typically assume Newtonian nonviscoelastic fluid flow conditions and incorporate melt viscosities that vary in complexity (i.e., ranging from a constant value to functional dependence on temperature and shear rate). Additional effects, such as solidification (evolving simultaneously with the cooling process), are often neglected.

1.2 Objective

The objective of the work is to model the FDM extrusion and deposition process at the mesoscale while including solidification effects and non-Newtonian viscoelastic flow conditions. It is intended that the model and simulation results will assist in further multiscale efforts at the microscale and macroscale. The models produced can assist in predictions regarding future testing efforts with varied inputs—particularly with respect to nozzle and extrusion velocities—and temperatures.

1.3 Approach and Scope

Restricting the work to a single line scan with a continuous extrusion flux of PLA polymer, the numerical simulations presented herein will be conducted with the assistance of the FEM-based multiphysics software COMSOL (COMSOL 2019) and incorporate a 2D heat and mass transfer analysis through a multiphase approach. The free surface, liquid–vapor interface will be simulated using a front-tracking, level-set method, and the melt viscosity will assume both temperature and shear rate dependency. Post-processing outcomes will focus on the evolving temperature, viscosity, and volume fraction and combine parametric studies associated with the various process control parameters to include nozzle and extrusion velocities as well as extrusion temperature. Initial benchmark applications focusing on an evolving melting front will serve to validate the heat transfer / phase change numerical framework.

2 Materials

The thermophysical material and rheological properties corresponding to PLA are shown in Table 1. As shown, several of the properties (λ, μ_0, n) relating to the viscosity are functions of temperature. Note that in this work, the thermal properties of PLA are constant for both liquid and solid phases. The operational parameters corresponding to extrusion velocity (V_e), extrusion temperature (T_e), scanning (nozzle) velocity (U_N), nozzle diameter (D_N), and standoff distance (h_s) are shown in Table 2 and include in certain cases (i.e. V_e, T_e, U_N) a range of values for purposes of parameterization studies.

Table 1. Thermophysical properties of PLA.

Property	Symbol	Value [unit]	Reference
Initial temperature	T_0	293.15 K	—
Thermal conductivity	k	0.195 $[\mathrm{W/(m \cdot K)}]$	Farah et al. 2016
Density	ρ	1,240 $[\mathrm{kg/m^3}]$	Le Marec et al. 2014
Specific heat (liquid)	C_p	2,000 $[\mathrm{J/(kg \cdot K)}]$	Le Marec et al. 2014
Surface tension coefficient	γ	0.04 [N/m]	Xia et al. 2017
Convective heat loss coefficient	h	20 $[\mathrm{W/(m^2 \cdot K)}]$	Xia et al. 2017
Latent heat of fusion	L_f	29.1E3 [J/kg]	Khoo et al. 2016
Zero shear rate viscosity	μ_0	$-0.473T^3 + 660.88T^2 - 307{,}833T + 5E{+}07$ [Pa· s]	Balani et al. 2019
Infinite shear rate viscosity	μ_∞	0 [Pa· s]	Balani et al. 2019
Relaxation time	λ	$5E{-}06T^3 - 0.0076T^2 + 3.5977T - 567.86$ [s]	Balani et al. 2019
Power index	n	$5E{-}05T^3 - 0.0676T^2 + 31.401T - 4861.4$	Balani et al. 2019
Coefficients in Darcy's law	c_1/c_2	1.6E3/1.0E-3	—
Melting temperature	T_m	438.15	Farah et al. 2016; Mehta et al. 2005
Transition zone temperature range	ε	50 K	—

Table 2. Operational parameters.

Property	Symbol	Value
Scanning (nozzle) velocity	U_{N}	0.10–0.20 m/s
Extrusion velocity	V_{e}	0.1–0.25 m/s
Extrusion temperature	T_{e}	463–473 K
Nozzle diameter	D_{N}	1.0 mm
Stand-off distance	h_{s}	$1.5D_{\mathrm{N}}$

3 Modeling/Simulation

3.1 Model Assumptions

The following assumptions were applied to the FDM model:

1. The geometry is assumed 2D with coordinates (x, y).
2. The surface tension coefficient (γ) is assumed constant, and therefore the Marangoni effect is neglected.
3. Heat losses due to vaporization and radiation effects are omitted since vaporization temperatures (~644 K) are not reached.
4. Model solidification assumes that the fluid flow within the transition zone (between solid and fluid) is similar to the flow in a porous media (i.e., we define a temperature-dependent porosity function $f_l(T)$).
5. A modified heat capacity is used within the energy equation (C_p^{eq}), which accounts for the latent heat of fusion
6. The liquid phase is assumed incompressible (density is assumed constant) and laminar.

3.2 FDM Model Equations

Subject to the above assumptions, the FDM model equations may be written as follows.

Energy:

$$\rho C_p \left(\frac{\partial T}{\partial t} + \nabla \cdot (\boldsymbol{u}T)\right) = k\nabla^2 T - h(T - T_0)\delta(\phi). \quad (1)$$

Mass:

$$\nabla \cdot \boldsymbol{u} = 0. \quad (2)$$

Momentum:

$$\rho \left(\frac{\partial \boldsymbol{u}}{\partial t} + \boldsymbol{u} \cdot \nabla \boldsymbol{u}\right) = \nabla \cdot [-p\boldsymbol{I} + \mu(\nabla \boldsymbol{u} + (\nabla \boldsymbol{u})^T)] + \rho \boldsymbol{g} + \boldsymbol{F}_s + +\gamma \boldsymbol{n} \kappa \delta(\phi), \quad (3)$$

where T is the temperature, $\boldsymbol{u}$ is the velocity, t is the time, ρ is the density, and k is the thermal conductivity. Additionally, p is the pressure, $\boldsymbol{I}$ is the identity matrix, κ is the curvature, $\boldsymbol{g}$ is the acceleration due to gravity, γ is the surface tension coefficient, ϕ is the level set variable, $\boldsymbol{n}$ is the interface

normal unit vector (where $\delta(\phi)$ is used to track the interface and is defined in Equation 5), $\boldsymbol{F}_{\mathrm{s}}$ is a momentum force due to solidification, and $(\nabla \boldsymbol{u})^T$ is the transposed vector of velocity gradients.

The conservation equations are complemented with a front-tracking method (in this case the level-set method) to track the solid–liquid–vapor interface. As opposed to other front-tracking methods, the level-set method uses a fixed mesh and dependent variable ϕ defined over the entire computational domain. In this work, ϕ is prescribed a value of 0 within the liquid (and solid phases) and a value of 1 within the vapor (air) phase. The dynamics of the interface, and the associated advection of ϕ, is determined in part from solutions of velocity. Further, the phase transition (represented by the prescribed thickness of the interface) is governed by a smooth step function, allowing for the mitigation of numerical divergence.

The evolution of ϕ may be expressed as

$$\frac{\partial \phi}{\partial t} + \boldsymbol{u} \cdot \nabla \phi = \gamma_{\mathrm{ls}} \nabla \cdot \left(\varepsilon_{\mathrm{ls}} \nabla \phi - \phi(1-\phi) \frac{\nabla \phi}{|\nabla \phi|} \right), \tag{4}$$

where γ_{ls}, and $\varepsilon_{\mathrm{ls}}$ are constants representing the distance of transition and speed of reinitialization, respectively. Additionally, the interface delta function (used to track the solid–liquid–vapor interface) may be expressed as

$$\delta(\phi) = 6|\phi(1-\phi)||\nabla \phi|. \tag{5}$$

3.2.1 Solidification

The solidification model used in this work is based on the model developed by Voller and Prakash (1987) and is used to compute the force $\boldsymbol{F}_{\mathrm{s}}$ shown in Equation 3. First, a temperature-dependent liquid fraction function ($f_l(T)$) is defined as follows:

$$f_{\mathrm{l}}(T) = \begin{cases} 0, T \geq (T_{\mathrm{m}} + \varepsilon) \\ \frac{(T_{\mathrm{m}} + \varepsilon - T)}{2\varepsilon}, (T_{\mathrm{m}} + \varepsilon) > T \geq (T_{\mathrm{m}} - \varepsilon), \\ 1, T < (T_{\mathrm{m}} - \varepsilon) \end{cases} \tag{6}$$

where T_m is the average melting temperature and 2ε represents the temperature of the transition zone, namely the temperature interval

between a purely liquid and solid phase. (Note that for pure materials, $\varepsilon = 0$).

An intermediate function, A, is then defined as

$$A = \frac{c_1(1-\psi)^3}{(\psi^3+c_2)}, \tag{7}$$

where $\psi = 1 - f_l(T)$, and c_1 and c_2 are constants (with c_1 and c_2 prescribed with comparatively large and small values, respectively). $\boldsymbol{F}_s$ may then be written as

$$\boldsymbol{F}_s = -A\boldsymbol{u}\phi, \tag{8}$$

where ϕ ensures that $\boldsymbol{F}_s$ acts only on the liquid phase and not the vapor phase.

Thus we see that when T is greater than $T_m + \varepsilon$ (i.e., greater than the liquidus temperature), $\psi = 1$ and $A = 0$, representing a fully fluid phase. However, when T is less than $T_m - \varepsilon$, $\psi = 0$, and $A = c_1/c_2$. If $c_1$is sufficiently large (with c_2 small), $\boldsymbol{F}_s$ dominates the convective and diffusive terms within the momentum equation (see Equation 3) and thus forces the velocity to become zero. For the intermediate case within the transition zone (i.e., $(T_m + \varepsilon) > T \geq (T_m - \varepsilon)$), $f_l(T)$ takes on a value between 0 and 1 and the flow behaves similar to that of a porous media.

Finally, to account for the latent heat of fusion of the polymer, a modified heat capacity equation is used:

$$C_{p,\mathrm{PLA}}^{eq} = C_{p,s} + L_f \frac{e^{-\left((T-T_m)^2/(T_l-T_s)^2\right)}}{\sqrt{\pi(T_l-T_s)^2}}, \tag{9}$$

where $T_l = T_m + \varepsilon$, $T_s = T_m - \varepsilon$, L_f is the latent heat of fusion, and $C_{p,s}$ is the solid phase, isobaric heat capacity.

The total heat capacity, accounting for both the air ($c_{p,a}$) and the polymer can then be written as

$$C_p = C_{p,a} + \left(C_{p,\mathrm{PLA}}^{eq} - C_{p,a}\right)\phi. \tag{10}$$

3.2.2 Viscosity

The polymer dynamic viscosity follows the non-Newtonian Carreau model (Masud and Kwack 2011; and Kim 2002), allowing for temperature and shear rate dependence, and is expressed as

$$\mu_{\mathrm{PLA}} = \mu_\infty + (\mu_0 - \mu_\infty)[1 + (\lambda\dot{\gamma})^2]^{\frac{n-1}{2}}, \tag{11}$$

where μ_0 and μ_∞ are the zero shear rate viscosity and infinite shear rate viscosity, respectively (note for this work $\mu_\infty = 0$), n is the power index, and λ is the relaxation time.

The shear rate, $\dot{\gamma}$, is expressed in terms of the rate of deformation tensor ($\boldsymbol{S}$):

$$\dot{\gamma} = \sqrt{2\boldsymbol{S}:\boldsymbol{S}}, \tag{12}$$

where

$$\boldsymbol{S} = \frac{1}{2}[\nabla\boldsymbol{u} + (\nabla\boldsymbol{u})^T]. \tag{13}$$

Finally, the total dynamic viscosity (μ), density (ρ), and thermal conductivity (κ) may be expressed as

$$\mu = \mu_{\mathrm{a}} + (\mu_{\mathrm{PLA}} - \mu_{\mathrm{a}})\phi, \tag{14}$$

$$\rho = \rho_{\mathrm{a}} + (\rho_{\mathrm{PLA}} - \rho_{\mathrm{a}})\phi, \tag{15}$$

$$\kappa = \kappa_{\mathrm{a}} + (\kappa_{\mathrm{PLA}} - \kappa_{\mathrm{a}})\phi. \tag{16}$$

3.3 Model Geometry and Initial/Boundary Conditions

The geometry and initial/boundary conditions are shown in Figure 1. With respect to the geometry, the magnitudes for the standoff distance (h_{s}) and nozzle diameter (D_{N}) are specified in Table 2. As indicated, the nozzle translates along the x-direction with a constant scanning speed (U_{N}) made feasible by the use of COMSOL's moving mesh facility (COMSOL 2019). The continuity boundary conditions along this moving interface assume an outward-directed, convective heat transfer, as well as a zero pressure condition. At the nozzle boundaries, the extrusion temperature (T_{e}) is

maintained over the total nozzle transit time. The remaining boundaries are prescribed as shown in Figure 1.

Figure 1. Computational domain, coordinate system reference, boundary, and initial conditions for the fused deposition modeling (FDM) model.

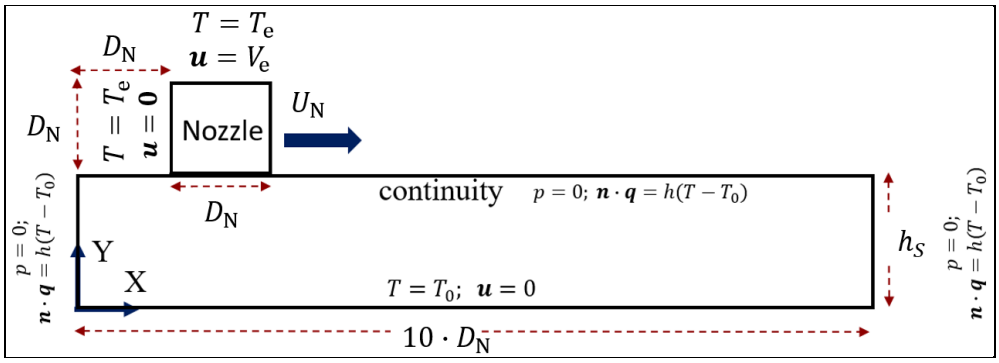

3.4 Solution Procedure

As stated previously, the FEM-based COMSOL multiphysics (COMSOL 2019) program was used to solve the aforementioned set of equations pertaining to the FDM model. Subsequent to meshing the 2D computational domain using a fine (Delaunay-based) distribution of triangular elements and assigning the input thermophysical properties and operation properties given in Table 1 and Table 2, respectively, the appropriate phase conditions were initialized using the level-set equation (Equation 4). The time-dependent analysis was then commenced, invoking Equations 1 through 4, which were solved in a fully coupled manner using adaptive time stepping. Additionally, a moving mesh was invoked at the continuity boundary, and the nozzle was prescribed a purely horizontal (x-direction) deformation according to:

$$d_x = U_N * t. \tag{17}$$

4 Results

4.1 Preliminary Model Validation

Preliminarily, and as a form of validation for the aforementioned equations applicable to heat transfer with phase change, a 1D benchmark application involving a melting front is considered (see Figure 2 [*left*]). This particular problem was selected due to the availability of an analytical solution (Hu and Argyropoulos 1996). Specifically, we consider a column of ice/water of length x = 1 m and initial temperature T_0=283 K subject to a fixed temperature of 253 K at its leftmost boundary (x = 0 m). The problem was discretized using 50 linear finite elements over a total simulation time of 72.0E3 s.

As shown in Figure 2 (*left*), the interface separating the frozen and liquid water is seen to transition from left to right. Figure 2 (*right*) also shows the excellent agreement between the current numerical model with the analytical results (Hu and Argyropoulos 1996).

Figure 2. Melting front example and temperature profiles along 1D domain, phase transition (*left*) and comparisons of current numerical and analytical solutions (Hu and Argyropoulos 1996) at t = 72.0E3 s (*right*).

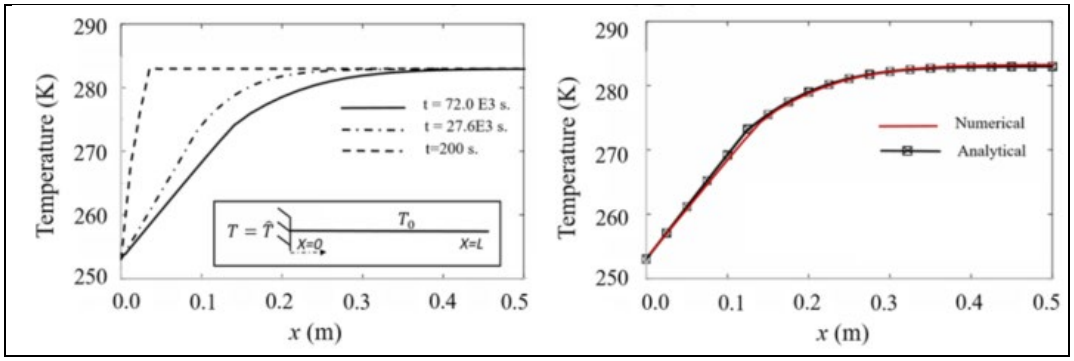

4.2 FDM Simulations

Figure 3 shows the time evolution of the PLA volume fraction over a time period of 0.12 s, which corresponds to a nozzle transit distance of approximately 80% of the total length of the underlying substrate. Here the surrounding vapor (air) phase is shown in red (i.e., ϕ = 1) while the extruded PLA liquid/solid phase is shown in blue (i.e., ϕ = 0). The interface region is clearly distinguished by the intermediate liquid–vapor color transition. As indicated (for the input properties specified), the

transiting nozzle extrudes the liquid PLA in a nearly continuous bead with a height of approximately 0.75 h_s.

Figure 3. Contour evolution of the polylactic acid (PLA) volume fraction ($U_N = 0.10$ m/s; $V_e = 0.20$ m/s; $T_e = 473$ K).

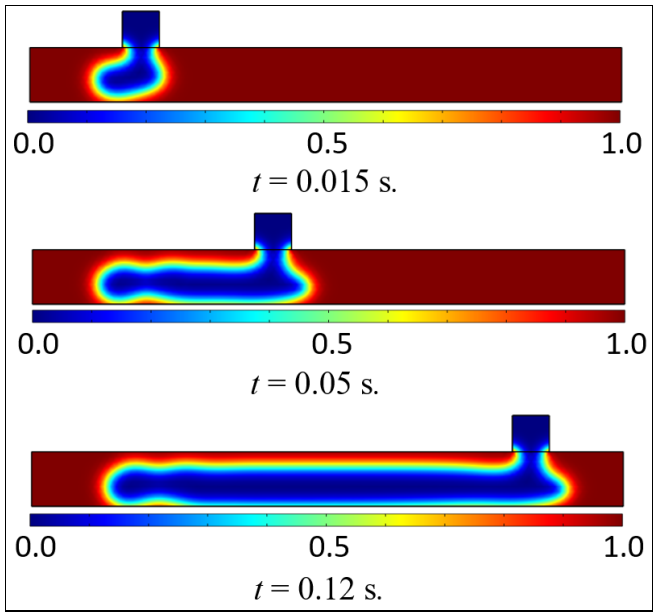

Figure 4 shows the effect of varying the extrusion velocity from 0.10 m/s to 0.25 m/s, with all other input conditions as prescribed in Table 1. As indicated, the PLA volume fraction becomes a series of irregularly spaced, disjointed circular discs for $V_e = 0.10$ m/s. At $V_e = 0.15$ m/s, and a continuous bead of height ~0.5h_s eventually develops subsequent to the formation of several discontinuous circular bead formations. Not until the extrusion velocity approaches 0.20 m/s (see Figure 4*c*) do we observe a nearly continuous uninterrupted PLA bead of height ~0.75h_s. Finally, for $V_e = 0.25$ m/s, the PLA bead height becomes nearly equivalent to h_s.

Figure 4. Effect of variable extrusion velocity on PLA volume fraction ($U_N = 0.10$ m/s; $T_e = 473$ K; $t = 0.12$ s).

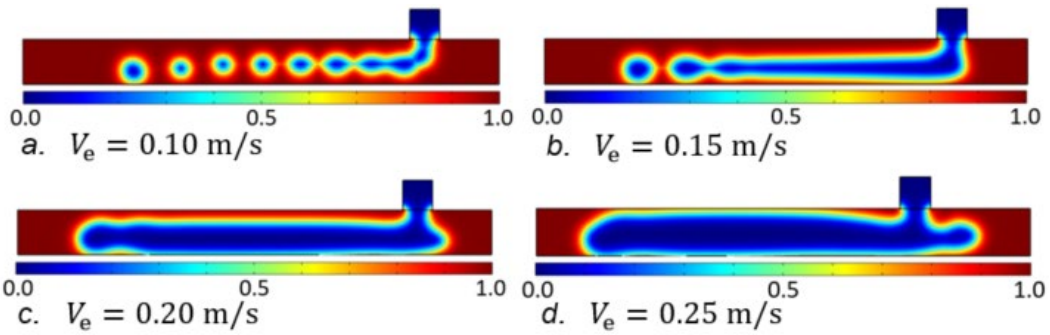

To quantify solidification effects, a series of additional parametric simulations were conducted relative to the evolution of the temperature and apparent viscosity. Specifically, these parametric studies considered variations in extrusion velocity (V_e) and nozzle velocity (U_N). The apparent viscosity (η), defined as $\eta = \tau/\dot{\gamma}$, was used (in lieu of dynamic or kinematic viscosity) in order to include the effects of shear rate ($\dot{\gamma}$). As the extruded PLA fluid begins to solidify, in addition to the expected reduction in temperature, there is also a concomitant increase in the apparent viscosity.

The results pertaining to the variation in V_e are show in Figure 5. In particular, four separate simulations were conducted with V_e ranging from 0.1 m/s to 0.25 m/s and with all other parameters as stated in Table 1. Precise measurements were considered at the location x = 3.7 mm, y = 0.35 mm. As indicated in Figure 5 (*left*), in addition to the expected decrease in temperature that occurs subsequent to the initial rapid increase in temperature (corresponding to the initial PLA extrusion from the nozzle), there also appears a strong dependence on V_e. In general, it is observed that smaller values of V_e correspond to lower values of temperature. As indicated, the largest decrease in temperature (~35 K) corresponds to $V_e = 0.10$ m/s. This result is reasonable given that the increase of V_e corresponds to an increase in mass flow rate (i.e., $\dot{m} \propto \rho V_e D_N$), thus a larger amount of energy is required for cooling purposes.

The results pertaining to η are shown in Figure 5 (*right*). Here η is observed to increase with decreasing values of V_e. As indicated, a maximum value of η = 5,000 Pa·s is achieved for both V_e = 0.1 m/s and V_e = 0.15 m/s relatively early on (at t = ~0.4 s in the case of V_e = 0.1 m/s). This relatively rapid increase in apparent viscosity is a result of the incongruous, circular PLA beads observed in Figure 4, which are more susceptible to the convective cooling effects than the continuous bead patterns observed for higher extrusion velocities and flow rates.

*Figure 5. Effect of variable extrusion velocity on temperature (left) and apparent viscosity (right) (**$U_N = 0.10\ m/s$**; **$T_e = 473\ K$**; t = 0.12 s.; measured at x = 3.7 mm, y = 0.35 mm).*

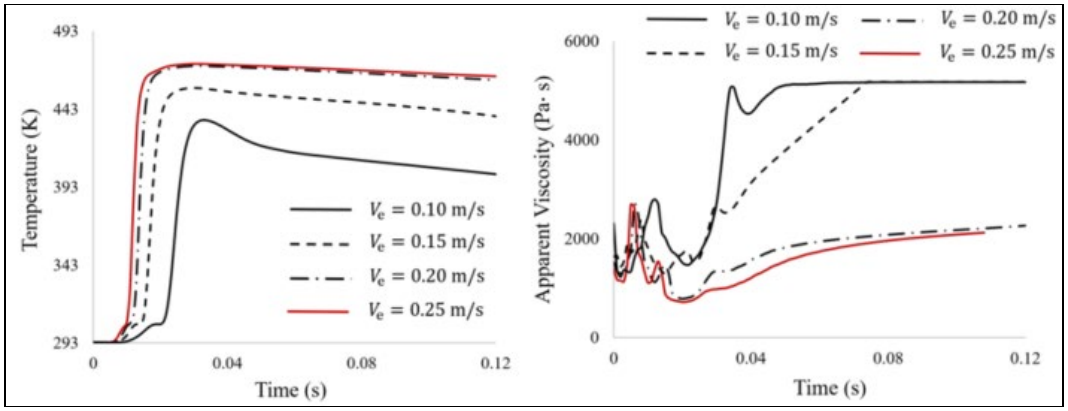

Figure 6 shows the results of variable nozzle velocity (U_N). In this case, three separate simulations were conducted for U_N ranging from 0.10 m/s to 0.20 m/s (with all other parameters as specified in Table 1 and Table 2). As indicted in Figure 6 (*left*), the local PLA temperature (measured at x = 3.7 mm, y = 0.35 mm) decreases for U_N = 0.20 m/s, while it remains approximately unvaried for U_N = 0.15 m/s and U_N = 0.10 m/s. The apparent viscosity (see Figure 6 [*right*]) is shown to achieve a maximum value of 5,000 Pa·s at 0.025 seconds for U_N = 0.20 m/s, while a gradual increase in apparent viscosity (reaching a maximum of approximately 2,500 Pa·s at t = 0.12 seconds) is observed for U_N = 0.15 m/s and U_N = 0.10 m/s.

Figure 6. Effect of variable nozzle velocity on temperature (*left*) and apparent viscosity (*right*) ($V_e = 0.20$ m/s; $T_e = 473$ K; t = 0.12 s.; measured at x = 3.7 mm, y = 0.35 mm).

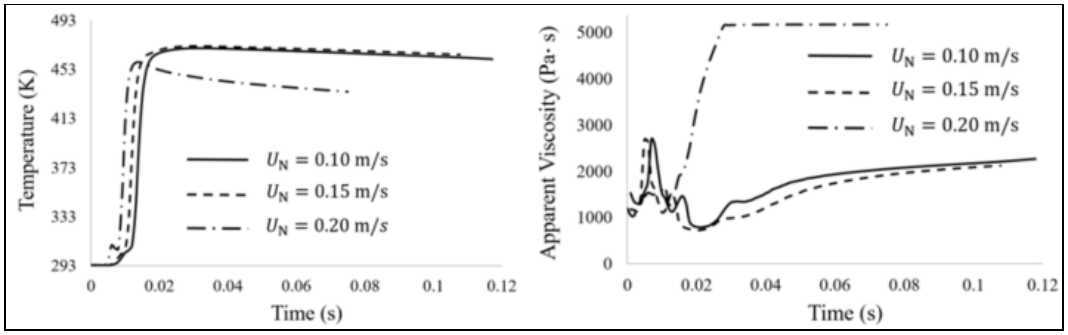

Finally, Figure 7 shows the results of variable extrusion temperature (T_e), ranging from 463 K to 473 K (with all other parameters as nominal per Table 1 and Table 2). From Figure 7 (*left*), the local PLA temperature (measured at x = 3.7 mm, y = 0.35 mm) marginally increases for increasing extrusion temperatures, with differences in magnitude nearly equivalent to the difference in extrusion temperature. In contrast, the apparent viscosity (see Figure 7 [*right*]) is shown to increase with

decreasing extrusion temperature, achieving a maximum value of 3,480 Pa·s at 0.025 seconds for T_e = 463 K.

Figure 7. Effect of variable extrusion temperature on temperature (*left*) and apparent viscosity (*right*) ($U_N = 0.10$ m/s; t = 0.12 s.; measured at x = 3.7 mm, y = 0.35 mm).

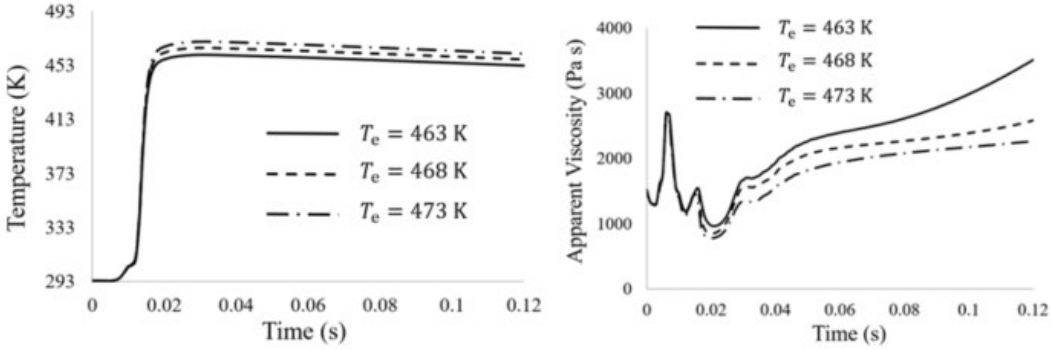

5 Conclusions

In this work we simulated the FDM mesoscale extrusion and deposition process with solidification effects. Restricting the work to a single line scan with a continuous extrusion flux of PLA polymer, the numerical simulations were conducted using COMSOL (COMSOL 2019) and incorporated a 2D heat and mass transfer analysis through a multi-phase approach. The free surface, liquid–vapor interface was simulated using a front-tracking, level-set method and the melt viscosity assumed both temperature and shear rate dependency. The results focused on the evolving temperature, viscosity, and volume fraction and were cast within a set of parametric studies associated with the nozzle and extrusion velocities, as well as the extrusion temperature. Some of the principal findings may be summarized as follows:

- FDM solidification can be effectively modeled using a front-tracking method (i.e., the level-set method) in concert with a temperature-dependent liquid fraction function (porosity function) and a modified heat capacity.
- Within the sampled parameter space, the continuity of the bead melt was largely dependent on the extrusion velocity, with discontinuities (or voids) observed for $V_e \leq 0.15$ m/s. This was further accompanied by an increase in solidification as quantified by the significant increase in apparent viscosity for $V_e \leq 0.15$ m/s.
- With respect to nozzle velocity, it was observed that a significant increase in apparent viscosity occurred for $U_N \geq 0.20$ m/s. Like the extrusion velocity, these velocities also corresponded to a discontinuous melt pattern.

References

Balani, S. B., F. Chabert, V. Nassiet, and A. Cantarel. 2019. "Influence of Printing Parameters on the Stability of Deposited Beads in Fused Filament Fabrication of Poly(lactic) Acid." *Additive Manufacturing* 25 (January): 112–21. https://doi.org/10.1016/j.addma.2018.10.012.

Comminal, R., M. P. Serdeczny, D. B. Pedersen, and J. Spangenberg. 2018. "Numerical Modeling of the Strand Deposition Flow in Extrusion-Based Additive Manufacturing." *Additive Manufacturing* 20 (March): 68–76. https://doi.org/10.1016/j.addma.2017.12.013.

COMSOL. 2019. *COMSOL Multiphysics Reference Manual, Version 5.5*. https://doc.comsol.com/5.5/doc/com.comsol.help.comsol/COMSOL_ReferenceManual.pdf.

Farah, S., D. G. Anderson, and R. Langer. 2016. "Physical and Mechanical Properties of PLA, and Their Functions in Widespread Applications—A Comprehensive Review." *Advanced Drug Delivery Reviews* 107 (December 15): 367–92. https://doi.org/10.1016/ j.addr.2016.06.012.

Heller, B., D. E. Smith, and D. A. Jack. 2016. "Effects of Extrudate Swell and Nozzle Geometry on Fiber Orientation in Fused Filament Fabrication Nozzle Flow." *Additive Manufacturing* 12 (October): 252–64. https://doi.org/10.1016/ j.addma.2016.06.005.

Hu, H., and S. A. Argyropoulos. 1996. "Mathematical modelling of solidification and melting: A Review," *Modelling and Simulation in Materials Science and Engineering* 4 (4): 371–96. Bristol, UK: IOP Publishing.

Khoo, R. Z., H. Ismail, and W. S. Chow. 2016. "Thermal and Morphological Properties of Poly (Lactic Acid) / Nanocellulose Nanocomposites." *Procedia Chemistry* 19: 788–94.

Kim, S. 2002. "A Study of Non-Newtonian Viscosity and Yield Stress of Blood in a Scanning Capillary-Tube Rheometer." PhD thesis. Philadelphia: Drexel University.

Le Marec, P. E., J.-C. Quantin, L. Ferry, J.-C. Benezet, S. Guilbert, and A. Bergeret. 2014. "Modelling of PLA Melt Rheology and Batch Mixing Energy Balance." *European Polymer Journal* 60: 273–85. https://doi.org/10.1016/j.eurpolymj.2014.09.012.

Masud, A., and J. Kwack. 2011. "A Stabilized Mixed Finite Element Method for the Incompressible Shear-Rate Dependent Non-Newtonian Fluids: Variational Multiscale Framework and Consistent Linearization." *Computational Methods in Applied Mechanical Engineering* 200 (5–8): 577–96. https://doi.org/10.1016/j.cma.2010.08.012.

Mehta, R., V. Kumar, H. Bhunia, and S. N. Upadhyay. 2005. "Synthesis of Poly (Lactic Acid): A Review." *Journal of Macromolecular Science, Part C: Polymer Reviews* 45 (4): 325–49.

Mohan, N., P. Senthil, S. Vinodh, and N. Jayanth. 2017. "A Review on Composite Materials and Process Parameters Optimization for the Fused Deposition Modelling Process." *Virtual and Physical Prototyping* 12: 47–59.

Mostafa, N., H. M. Syed, S. Igor, and G. Andrew. 2009. "A Study of Melt Flow Analysis of an ABS-Iron Composite in Fused Deposition Modelling Process." *Tsinghua Science and Technology* 14 (S1): 29–37.

Nikzad, M., S. Masood, and I. Sbarski. 2011. "Thermo-Mechanical Properties of a Highly Filled Polymeric Composites for Fused Deposition Modeling." *Materials and Design* 32 (6): 3448–56. https://doi.org/10.1016/j.matdes.2011.01.056.

Ramanath, H. S., C. K. Chua, K. F. Leong, and K. D. Shah. 2007. "Melt Flow Behavior of Poly-ε-Caprolactone in Fused Deposition Modelling." *Journal of Material Science and Materials Electronics* 19 (7): 2541–50.

Serdeczny, M. P., R. Comminal, D. B. Pedersen, and J. Spangenberg. 2018. "Experimental Validation of a Numerical Model for the Strand Shape in Material Extrusion Additive Manufacturing." *Additive Manufacturing* 24 (December): 145–53. https://doi.org/10.1016/j.addma.2018.09.022.

Sun, Q., G. M. Rizvi, C. T. Bellehumeur, and P. Gu. 2003. "Experimental Study of the Cooling Characteristics of Polymer Filaments in FDM and Impact on the Mesostructures and Properties of Prototypes." *Solid Freeform Fabrication Symposium*, Austin, TX.

Turner, B. N., R. Strong, and S. A. Gold. 2014. "A Review of Melt Extrusion Additive Manufacturing Processes: I. Process Design and Modeling." *Rapid Prototyping Journal* 20 (3): 192–204. https://doi.org/10.1108/RPJ-01-2013-0012.

Voller, V. R., and C. Prakash. 1987. "A Fixed Grid Numerical Modelling Methodology for Convection-Diffusion Mushy Region Phase Change Problems." *Journal of Heat and Mass Transfer* 30 (8): 1709–19. https://doi.org/10.1016/0017-9310(87)90317-6.

Wickramasinghe, S., T. Do, and P. Tran. 2020. "FDM-Based 3D Printing of Polymer and Associated Composite: A Review on Mechanical Properties, Defects and Treatments." *Polymers* 12 (7): 1529.

Xia, H., F. Lu, S. Dabiri, and G. Trykggvason. 2017. "Fully Resolved Numerical Simulations of Fused Deposition Modeling. Part I: Fluid Flow." *Rapid Prototyping Journal* 24 (2): 463–76. https://doi.org/10.48550/arXiv.1711.05940.

Ziemian, C., M. Sharma, and S. Ziemian. 2012. "Anisotropic Mechanical Properties of ABS Parts Fabricated by Fused Deposition Modelling." In M. Gokcek (ed.), *Mechanical Engineering*. London: InTech, 159–80.

REPORT DOCUMENTATION PAGE

1. REPORT DATE	2. REPORT TYPE	3. DATES COVERED	
May 2024	Technical report	START DATE FY22	END DATE FY23

4. TITLE AND SUBTITLE

Mesoscale Multiphysics Simulations of the Fused Deposition Additive Manufacturing Process

5a. CONTRACT NUMBER	5b. GRANT NUMBER	5c. PROGRAM ELEMENT
5d. PROJECT NUMBER	**5e. TASK NUMBER**	**5f. WORK UNIT NUMBER**

6. AUTHOR(S)

Jeff Allen and Guillermo Riveros

7. PERFORMING ORGANIZATION NAME(S) AND ADDRESS(ES)

US Army Engineer Research and Development Center
Information Technology Laboratory (ITL)
3909 Halls Ferry Road
Vicksburg, MS 39180-6199

8. PERFORMING ORGANIZATION REPORT NUMBER

ERDC/ITL TR-24-7

9. SPONSORING/MONITORING AGENCY NAME(S) AND ADDRESS(ES)

US Army Engineer Research and Development Center
Information Technology Laboratory
3909 Halls Ferry Rd
Vicksburg, MS 39180-6199

10. SPONSOR/MONITOR'S ACRONYM(S)

HQUSACE

11. SPONSOR/MONITOR'S REPORT NUMBER(S)

12. DISTRIBUTION/AVAILABILITY STATEMENT

Distribution Statement A. Approved for public release: distribution is unlimited.

13. SUPPLEMENTARY NOTES

Funding Account Code U4393864, AMSCO Code 633043DC300

14. ABSTRACT

As part of an ongoing effort to better understand the multiscale effects of fused deposition additive manufacturing, this work centers on a multiphysics, mesoscale approach for the simulation of the extrusion and solidification processes associated with fused deposition modeling. Restricting the work to a single line scan, we focus on the application of polylactic acid. In addition to heat, momentum, and mass transfer, the solid–liquid–vapor interface is simulated using a front-tracking, level-set method. The results focus on the evolving temperature, viscosity, and volume fraction and are cast within a set of parametric studies to include the nozzle and extrusion velocities as well as the extrusion temperature. Among other findings, it was observed that fused deposition modeling can be effectively modeled using a front-tracking method (i.e., the level-set method) in concert with a moving mesh and temperature-dependent porosity function.

15. SUBJECT TERMS

Additive manufacturing; Multiscale modeling; Polylactic acid; Three-dimensional printing

16. SECURITY CLASSIFICATION OF:			17. LIMITATION OF ABSTRACT	18. NUMBER OF PAGES
a. REPORT	b. ABSTRACT	C. THIS PAGE		
Unclassified	Unclassified	Unclassified	SAR	26

19a. NAME OF RESPONSIBLE PERSON	19b. TELEPHONE NUMBER (include area code)